

A New Porous Metallic Carbon Allotrope with Interlocking Pentagons for Sodium-Ion Battery Anode Material

Dongyuan Ni, Yaguang Guo, Yupeng Shen, and Qian Wang*

The high rate performance of metal-ion batteries requires the anode to be conductive not just ionically but also electronically. This criterion has significantly stimulated study on porous metallic carbon with intrinsically high electron conductivity. In contrast to the previously reported metallic T6-carbon constructed by interlocking carbon hexagons, here a new 3D metallic carbon composed of interlocking carbon pentagons, penta-h22, is proposed. Based on state-of-the-art theoretical calculations, it is shown that penta-h22 is energetically more stable than T6-carbon. More importantly, different from T6-carbon with too small pores for metal ions, penta-h22 possesses a large specific capacity of 609 mAh g⁻¹, low diffusion barrier of 0.20 eV, low open-circuit voltage of 0.63 V, and small volume change of 1.75%. These parameters clearly indicate that pentagon-based 3D porous carbon is promising for the anode of Na-ion batteries.

It is important to note that metallic and semimetallic carbon structures are promising candidates for anode materials of metal-ion batteries due to their intrinsically high carrier mobility.^[2,18–21] However, the interlocking hexagonal T6-carbon is not suitable for this task due to its small pores. Motivated by the recent theoretical prediction^[22–24] and experimental synthesis of 3D graphene monoliths by assembling graphene nanoribbons,^[25] which exhibit great potential for alkali-ion battery anode materials because of their porosity and metallicity.^[2,26] Here, we propose a new 3D porous carbon by using a trifoliolate-unit composed of three interlocking pentagons as the building block, and find that this novel structure, called penta-h22, is indeed metallic and energetically more stable than T6-carbon, and

shows high performance as an anode material for sodium-ion batteries (SIBs).

1. Introduction

Carbon, due to its flexible bonding and hybridization features, has formed a big family with various allotropes^[1,2] from the well-known diamond, graphite, to the low-dimensional materials such as graphene,^[3] carbon nanotube,^[4] and C₆₀ fullerene,^[5] exhibiting intriguing atomic configurations and fascinating properties. Among them, metallic carbon has received increased attention because of its wide applications in many areas including superconductivity,^[6,7] electron–phonon coupling,^[8,9] phonon–plasmon coupling,^[10] catalysis,^[11] and spintronics.^[12] In previous study,^[13] we showed that a stable 3D metallic carbon (called T6-carbon) can be designed by interlocking hexagonal carbon rings. While besides hexagons, pentagons are also basic structural units of carbon allotropes as evidenced by C₂₀ fullerene,^[14,15] penta-graphene,^[16] and 3D chiral pentagonal structures (CHIPODS).^[17] Therefore, we explore the possibility of designing a stable 3D porous metallic carbon by interlocking pentagons.

2. Computational Methods

All the calculations are performed based on density functional theory (DFT) implemented in the Vienna Ab initio Simulation Package.^[27] The exchange-correlation energy is described by the generalized gradient approximation with the Perdew–Burke–Ernzerhof (PBE) form.^[28] The projector augmented wave method is used to treat the interactions between ion cores and valence electrons with a plane-wave energy cutoff of 800 eV. In addition, the Heyd–Scuseria–Ernzerhof (HSE06)^[29] hybrid functional is used to get more accurate electronic band structure. For geometry optimization, the convergence criteria for the total energy and force on each atom are set to be 10⁻⁴ eV and 10⁻³ eV Å⁻¹, respectively. The first Brillouin zone is sampled using 3 × 3 × 7 Monkhorst–Pack *k*-point scheme.^[30] The high symmetry *k*-point path is generated by using AFLOW software.^[31] The phonon spectrum is calculated by using the finite-displacement method^[32,33] in a 1 × 1 × 3 supercell with a 3 × 3 × 3 *k*-mesh. The thermal stability is confirmed by using ab initio molecular dynamics (AIMD) simulations with the canonical ensemble in Nosé thermostat.^[34] The diffusion energy barrier profile is studied by the climbing-image nudged elastic band (CI-NEB) method.^[35] The effect of van der Waals interactions are included by using the PBE-D2 functional^[36] for adsorption and diffusion of Na ions.

D. Ni, Dr. Y. Guo, Y. Shen, Prof. Q. Wang
Center for Applied Physics and Technology, HEDPS
School of Materials Science and Engineering
BKL-MEMD
Peking University
Beijing 100871, China
E-mail: qianwang2@pku.edu.cn

 The ORCID identification number(s) for the author(s) of this article can be found under <https://doi.org/10.1002/adts.202100025>

DOI: 10.1002/adts.202100025

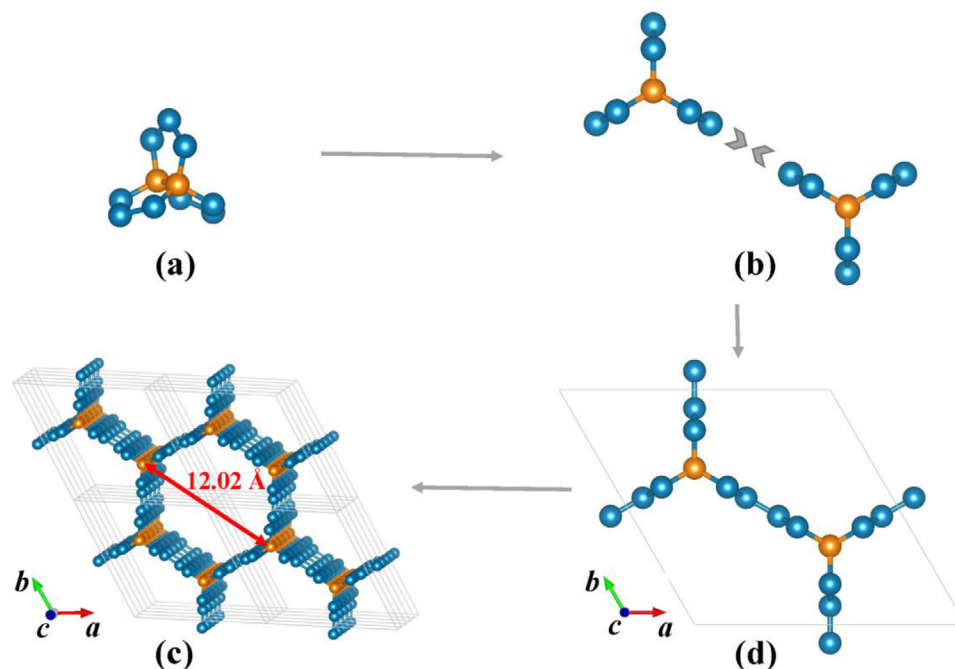


Figure 1. a) Trifoliolate-unit formed by interlocking three pentagons. b) Assembling process between two trifoliolate-units. c) Optimized geometry of the porous 3D interlocking pentagon structure and d) its unit cell. The blue and orange spheres represent the sp^2 - and sp^3 -hybridized carbon atoms, respectively.

3. Results and Discussion

3.1. Structure and Stability

The new 3D structure with interlocking pentagons is constructed via the following clue, shown in **Figure 1**. A building block of the trifoliolate-unit is first formed by interlocking three pentagons, and then a hexagonal unit cell containing 22 carbon atoms of the 3D crystal is built by tailoring assembly of the trifoliolate-units. We name it penta-h22. The optimized structure of penta-h22 has $P6/mmm$ symmetry with the lattice parameters of $a = b = 10.41$ Å and $c = 3.74$ Å. In this structure, there are three chemically nonequivalent carbon atoms, i.e., 6m (0.920, 0.460, 0.500), 12o (0.828, 0.414, 0.814), and 4h (0.333, 0.667, 0.694). The 4h atoms are in sp^3 -hybridization and the others are sp^2 -hybridized. As shown in **Figure 1c**, there is a large channel with a diameter of 12.02 Å along the c direction, leading to a density of 1.25 g cm^{-3} , which is lower than that of many other carbon allotropes such as graphite (2.24 g cm^{-3}) and hexagonal zigzag graphene monolith (HZGM-42) (1.39 g cm^{-3}).^[24]

To study the energetic stability of penta-h22, we calculate its binding energy and compare the binding energy with that of some other 3D carbon allotropes, including diamond, graphite, T6,^[13,37,38] H₁₈,^[39] Tri-C₉,^[40] and K6^[41] carbons. As shown in **Figure 2a**, except for diamond and graphite, penta-h22 has the lowest energy, especially lower than that of T6 carbon by 0.19 eV per atom at their equilibrium configurations. To study the dynamic stability, we calculate its phonon spectrum as shown in **Figure 2b**. The absence of imaginary modes in the first Brillouin zone confirms the dynamic stability of penta-h22. In addition, the acoustic branches and most of the optical branches show larger

slopes in the Γ -A path as compared with those in the Γ -M and Γ -K paths. The large slope corresponds to high group velocities of phonons along the c direction, which would favor a high thermal conductivity. Furthermore, the thermal stability is examined by increasing temperature gradually from 300 to 1200 K for 10 ps with a time step of 1 fs using AIMD simulation. To reduce the influence of the periodic boundary condition, we use a supercell of $1 \times 1 \times 3$. As shown in **Figure 2c,d**, the total potential energy fluctuates slightly around the average value and the structural skeleton remains almost intact at the end of the AIMD simulation at 1200 K, indicating that penta-h22 is thermally stable at temperature as high as 1200 K.

To verify the mechanical stability of penta-h22, we calculate the linear elastic constants by using the energy-strain method implemented in the AELAS software,^[42,43] i.e., calculating the quadratic coefficients by fitting the energy-strain relationship. The elastic constants of penta-h22 and other promising anode candidates including HZGM-42,^[24] hC28^[23] are listed in **Table 1** for comparison. One can see that penta-h22 exhibits a larger elastic constant (C_{33}) of 635.9 GPa along the c -direction as compared to hC28 (591.4 GPa), implying its stiffness is high in this direction. While the elastic constant (C_{11} , C_{13} , and C_{44}) are smaller than those of both HZGM-42 and hC28 because of its large pores in the hexagonal channels. For a hexagonal lattice, there are only five independent elastic constants, i.e., C_{11} , C_{12} , C_{13} , C_{33} , and C_{44} . According to Born-Huang criteria^[44] for a 3D hexagonal lattice, the following conditions have to be obeyed: $C_{11} > |C_{12}|$, $2C_{13}^2 < C_{33}(C_{11} + C_{12})$, and $C_{44} > 0$. We find that the calculated linear elastic constants of penta-h22 satisfy all of the above conditions, confirming that penta-h22 is mechanically stable.

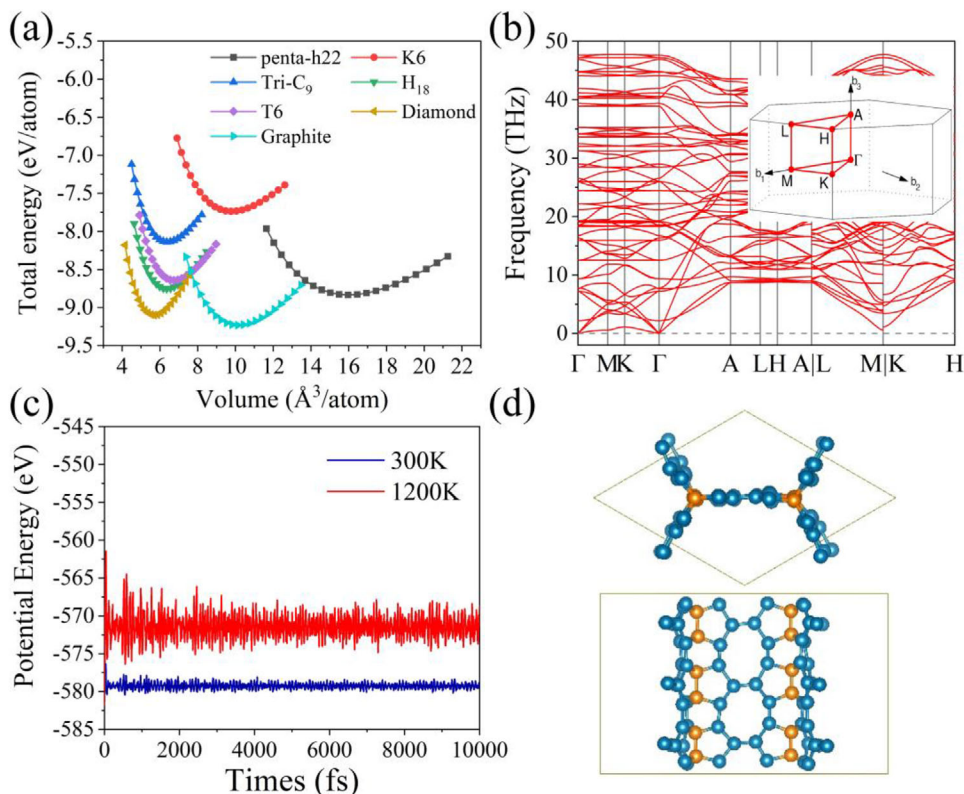


Figure 2. a) Energy comparison and b) phonon spectrum of penta-h22 along the high symmetry q -point path in the first Brillouin zone. c) Energy fluctuation during the AIMD simulations at 300 and 1200 K, respectively. d) Top and side views of the atomic configuration of penta-h22 at the end of AIMD simulation at 1200 K.

Table 1. Calculated elastic constants (C_{ij} in GPa), Young's moduli (Y_i in GPa), and Poisson's ratios (ν_{ij}) of penta-h22 compared with other two honeycomb-structural carbon allotropes: HZGM-42 and hC28.

	Penta-h22	HZGM-42 ^[24]	hC28 ^[23]
C_{11}	143.3	198.0	157.5
C_{12}	125.5	86.5	147.9
C_{13}	39.5	56.3	47.7
C_{33}	635.9	637.7	591.4
C_{44}	85.0	138.4	103.5
Y_a	33.4	158.6	18.6
Y_b	33.4	158.6	18.6
Y_c	624.3	615.4	576.5
ν_{ab}	0.87	0.42	0.94
ν_{ac}	0.01	0.05	0.01
ν_{ba}	0.87	0.42	0.94
ν_{bc}	0.01	0.05	0.01
ν_{ca}	0.15	0.20	0.16
ν_{cb}	0.15	0.20	0.16

In addition, the mechanical properties of penta-h22 can also be derived. The Young's modulus (Y) and Poisson's ratio (ν) of penta-h22 are calculated by using the formulas^[45]

$$Y(n) = (s_{11}(1 - n_3^2)^2 + s_{33}n_3^4 + (2s_{13} + s_{44})(1 - n_3^2)n_3^2)^{-1} \quad (1)$$

and

$$\nu(n, m) = -Y(n)(s_{12}(m_1n_2 - m_2n_1)^2 + (s_{11} + s_{33} - 2s_{13} - s_{44})m_3^2n_3^2 + s_{13}(m_3^2 + n_3^2)) \quad (2)$$

here S_{ij} s are the elastic compliances, \mathbf{m} and \mathbf{n} are lattice vectors, and the corresponding lattice vectors are labeled in Figure 1c,d. The calculated results are also presented in Table 1, which show that penta-h22 is highly mechanically anisotropic, similar to HZGM-42 and hC28, but possesses a larger Young's modulus (624.3 GPa) than HZGM-42 (615.4 GPa) and hC28 (576.5 GPa) along the c direction. The values of Poisson's ratios are comparable to those of hC28 in all the directions. While different from penta-graphene with a negative Poisson's ratio, penta-h22 has positive Poisson's ratios due to the different arrangement of pentagons in its geometric structure.^[16]

To gain a better understanding of the mechanical strength of penta-h22, we further study the maximum stress by using the quasi-static displacement-controlled deformation method, which deforms the lattice with increasing strains along different directions.^[46] The stress-strain curves of penta-h22 along the x , y , and z directions are plotted in Figure 3. For comparison, the calculations are also performed for hC28^[23] and the results are

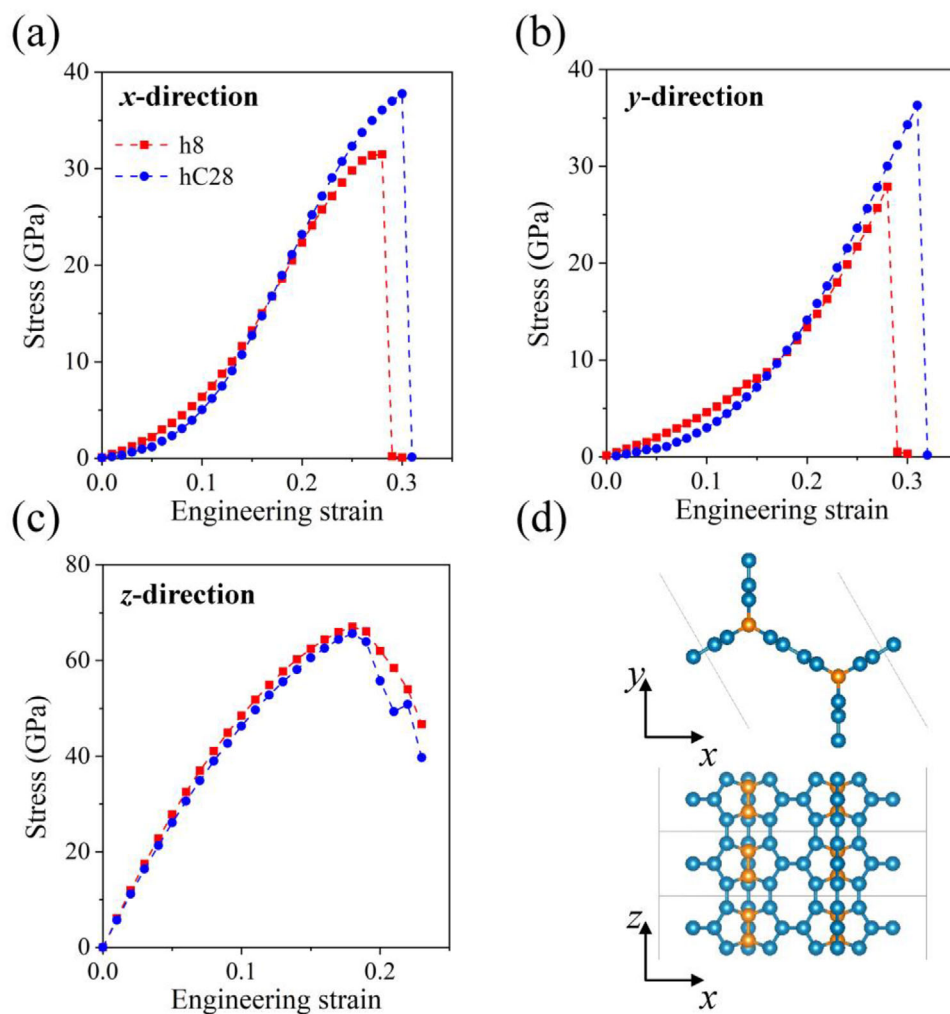


Figure 3. The stress–strain relationships for the tensile deformations of penta-h22 and hC28 along a) x , b) y , and c) z directions. d) The coordinate system in penta-h22.

given in Figure 3 as well. One can see that penta-h22 exhibits a slightly larger slope than that of hC28 near the zero strain point in the z -direction, corresponding to a higher Y_c of penta-h22, being consistent with the result in Table 1, which also suggests that penta-h22 possesses better ductility. Penta-h22 can sustain large strains of 0.28, 0.28, and 0.18 along the x , y , and z directions, respectively.

3.2. Electronic Properties

To examine the electronic properties of penta-h22, the band structure is calculated by using the PBE functional, as plotted in Figure 4a (blue lines). One can see that the conduction bands cross the Fermi level in the Γ –A path, suggesting that penta-h22 is metallic. This feature is further confirmed by our calculated results at the HSE06 level, in which the electron Coulomb screening is treated more accurately, also shown in Figure 4a (orange lines). The projected density of states (DOS) on the sp^2 and sp^3 -hybridized atoms (see Figure 4a) shows that the metallicity pri-

marily comes from the sp^2 -hybridized carbon atoms as the states near the Fermi level are mainly contributed by them. In addition, we calculate the electron localization function (ELF),^[47] which can be used as a measure of electron localization. The ELF values are renormalized between 0.0 and 1.0, while the value of 0.0 corresponds to a very low charge density, 1.0 refers to fully localized electrons, and 0.5 represents that the electrons are fully delocalized. The calculated ELF results for the two planes of penta-h22 are plotted in Figure 4b. The channels with ELF around the value of 0.5 along the sp^2 -carbon chains are marked by red rectangles, which indicates the electrons are fully delocalized and forms conducting channels along c direction, confirming the metallic character of penta-h22.

3.3. Applications as an Anode Material for SIBs

Due to the unique geometric configuration with regularly distributed channels and intrinsic metallicity, we study penta-h22 as an anode of metal-ion batteries. We take SIB as an example

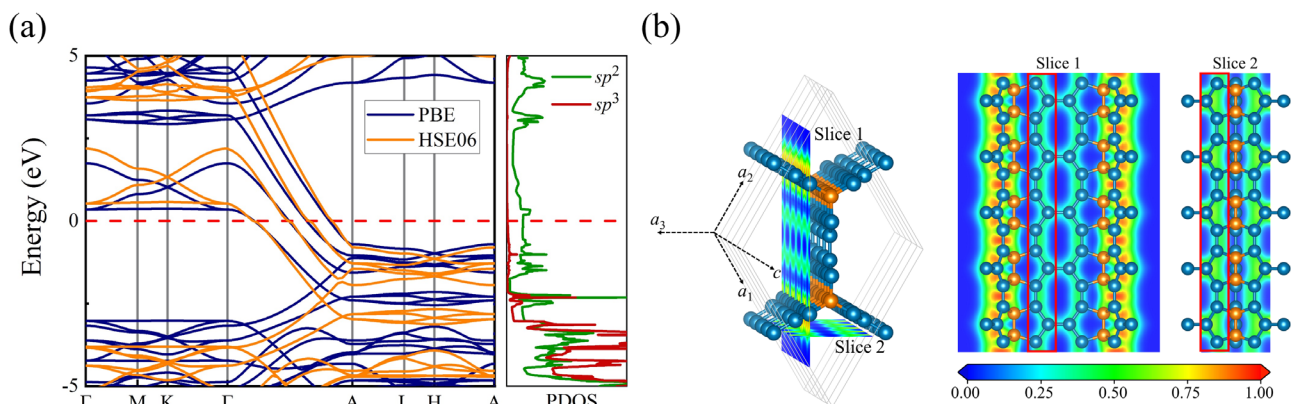


Figure 4. a) Electronic band structure calculated at the PBE (blue line) and the HSE06 (orange line) levels, respectively, and the projected DOS for the sp^2 and sp^3 -hybridized carbon atoms. b) Slices of ELF of penta-h22 on shifted lattice planes ($11\bar{2}0$) and ($1\bar{1}00$).

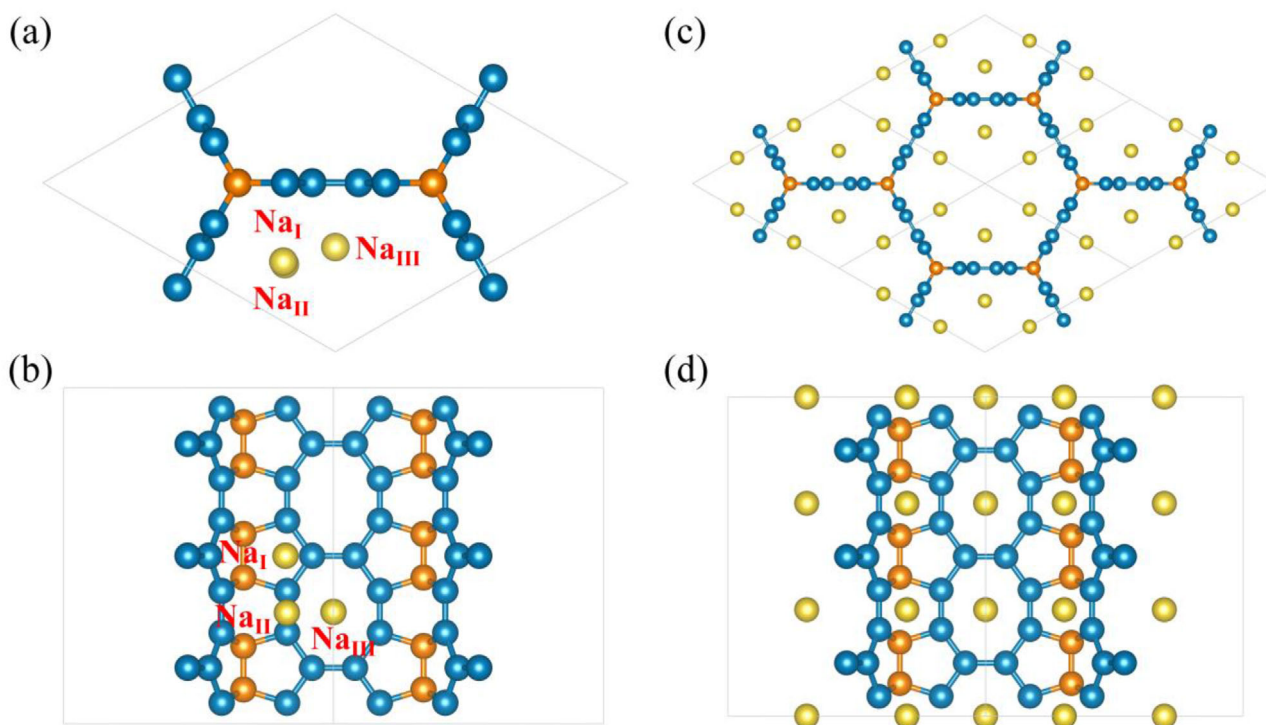


Figure 5. a,b) Top and side views of the possible Na adsorption sites. c,d) Top and side views of the fully Na-intercalated configuration of penta-h22. The blue, orange, and yellow spheres represent the sp^2 -, sp^3 -hybridized carbon atoms, and Na ions, respectively.

because many anode materials used in lithium-ion batteries (LIBs) are not suitable for Na-ion intercalation due to the large radii of Na ions, while SIB is considered as one of the potential substitutes to LIB. Therefore, the development of stable anode materials for SIBs with high reversible capacity and good rate capability is challenging and is of important significance. Hence, we systematically explore the potential of penta-h22 as an SIB anode by investigating its binding and diffusion behavior, including specific capacity, diffusion energy barriers, voltage profile, and volume change.

We first study the possible adsorption sites of penta-h22. The $1 \times 1 \times 3$ supercell is used to avoid Na-ions interaction. The effect of the vdW interaction is taken into account by utilizing the semiempirical long-range dispersion correction with the PBE-D2 functional.^[36] The large channels could provide space for storage and transport of Na-ions. Three possible adsorption sites are examined with high symmetry, named Na_I , Na_{II} , and Na_{III} , corresponding to the pentagonal hollow site, the C-C bridge site, and the large eight-membered-ring hollow site, respectively, as shown in **Figure 5a,b**. We calculate the binding energy of

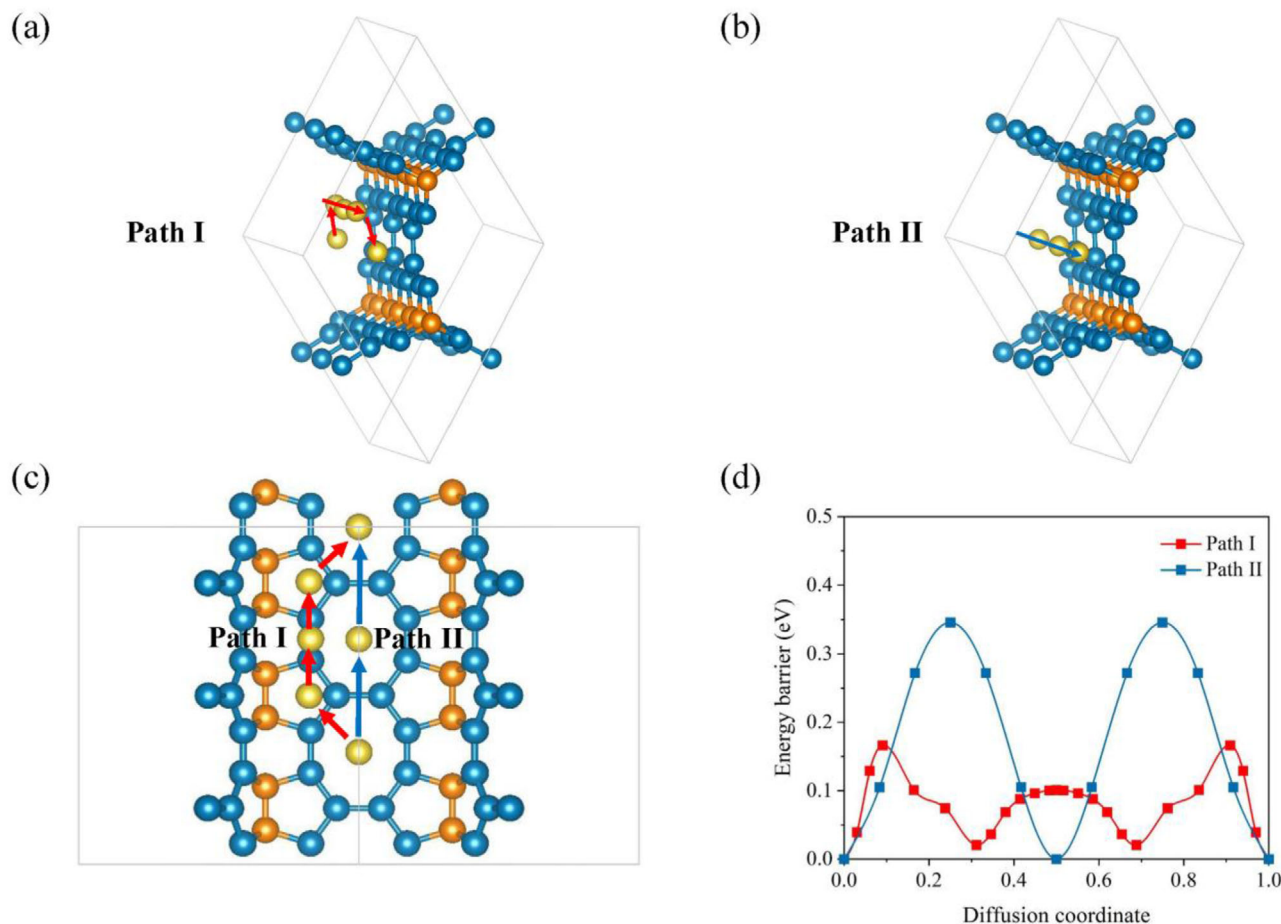


Figure 6. Perspective views of two migration paths of Na-ion diffusions, i.e., a) Path I (red arrows), b) Path II (blue arrows), and c) side view of two migration paths. d) Diffusion energy profiles of the two paths.

single-Na adsorption to verify the feasibility of three sites by using the following equation

$$E_b = \frac{(E_{\text{Na}_x\text{-penta-h22}} - E_{\text{penta-h22}} - x\mu_{\text{Na}})}{x} \quad (3)$$

where $E_{\text{Na}_x\text{-penta-h22}}$ and $E_{\text{penta-h22}}$ represent the energy of Na-inserted and pristine penta-h22 structures, respectively. The μ_{Na} is the energy of one Na atom in Na bulk. The binding energies on Na_I , Na_{II} , and Na_{III} are -1.03 , -0.95 , and -1.05 eV, respectively, suggesting that the Na_{III} site is the most energy-favorable site. To further probe the adsorption process, the Bader charge analysis^[48] is used to check electrons transfer. The result shows that all the Na atoms transfer 0.88 electrons to the carbon system in three adsorption conditions, implying the strong adsorptions of Na in penta-h22. On the other hand, the strong Coulomb repulsions between Na ions also prevent them from clustering.

The diffusion energy barrier is one of the important factors describing the mobility of Na ions. Due to the honeycomb structure of penta-h22, Na ions must migrate in separate channels, thus there are two possible migration paths for Na-ion diffusion along the c direction, as shown in **Figure 6a–c**. Path I is a circuitous route, while Path II corresponds to the direct migration of Na ions

along the channel. We calculate the energy barrier by using CI-NEB method.^[35] The calculated results are plotted in **Figure 6d**, which shows that the highest energy barriers for the two paths are 0.17 and 0.35 eV, respectively, the corresponding diffusion constant (D) can be calculated from the Arrhenius equation^[49]

$$D \propto \exp\left(-\frac{E_a}{K_B T}\right) \quad (4)$$

here E_a , K_B , and T represent the energy barrier, Boltzmann constant, and temperature, respectively. At room temperature ($T = 300$ K), the diffusion constant of Path I (energy barrier = 0.17 eV) is 1057 times higher than that of Path II (energy barrier = 0.35 eV). Therefore, Path I is much more favorable for Na-ion migration.

Next, the theoretical capacity of penta-h22 is studied by gradually adding Na atoms until reaching the fully Na-intercalation configuration as shown in **Figure 5c,d**. In this configuration, all of the Na_{III} sites are occupied. The average adsorption energy is calculated to be -0.63 eV, indicating that the clustering of Na ions does not occur even in such a high concentration (a supercell of 66 carbon atoms could insert 18 sodium ions). The specific capacity is 609 mAh g^{-1} ($\text{NaC}_{3.67}$), which is much higher than

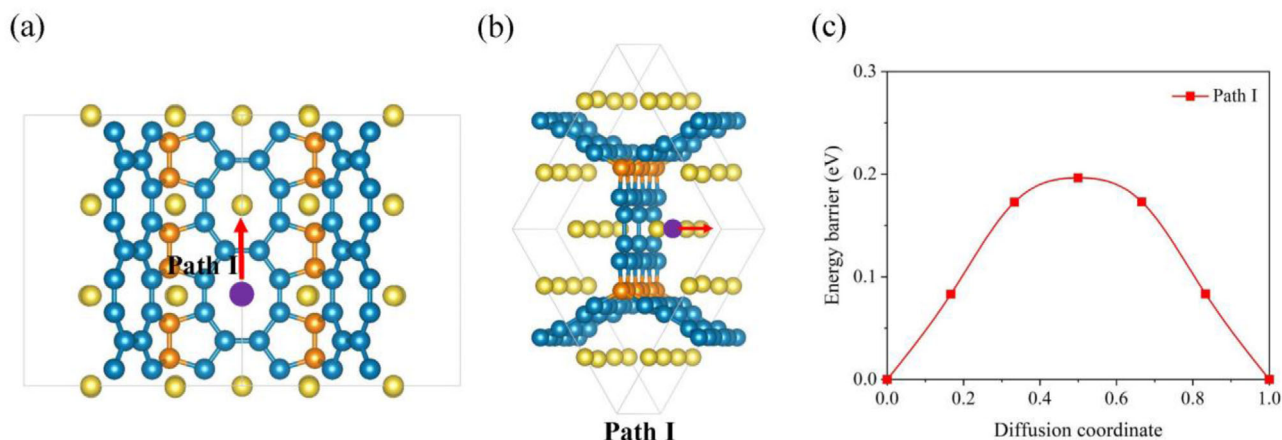


Figure 7. a) Side and b) top views of the migration path of vacancies diffusions. c) Energy profile of the migration path of the vacancy.

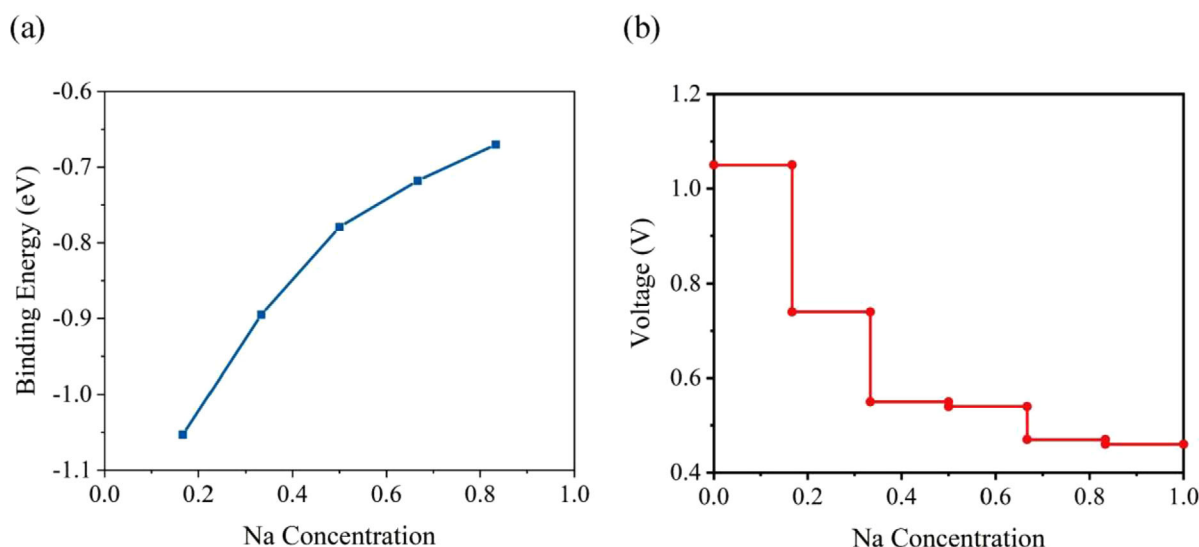


Figure 8. a) Binding energy (left) and b) voltage profile (right) of the five stable intermediate Na-concentration configurations.

that of tC_{24} ($232.65 \text{ mAh g}^{-1}$)^[50] and interpenetrating silicene networks (ISN) (159.5 mAh g^{-1}).^[51]

To calculate the diffusion barrier in the condition of high Na concentration, we remove one Na atom from the fully Na-intercalation configuration and employ CI-NEB to simulate the diffusion of vacancy as plotted in **Figure 7**. There is only one diffusion path for vacancies, since the Na ions only occupy the Na_{III} sites in the fully adsorbed configuration. The energy barrier is 0.20 eV at this concentration for Na ions, which indicates the Na ions can migrate easily even at high Na-concentration configurations.

The average open-circuit voltage (OCV) for penta-h22 is defined as

$$V \approx -\frac{E_{Na_{x_2}\text{-penta-h22}} - E_{Na_{x_1}\text{-penta-h22}} - (x_2 - x_1)E_{Na}}{(x_2 - x_1)e} \quad (5)$$

where $E_{Na_{x_2}\text{-penta-h22}}$, $E_{Na_{x_1}\text{-penta-h22}}$, and E_{Na} are the total energy of Na_{x_2} -intercalated penta-h22, Na_{x_1} -intercalated penta-h22,

and one single Na atom in bulk phase, respectively. To obtain energies at certain concentrations, five intermediate concentrations ($Na_xC_{3.67}$, $x = 0.167, 0.333, 0.500, 0.667,$ and 0.833) are studied. For each concentration, 15 symmetry-inequivalent structures are explored by using the Eward energy method implemented by pymatgen software^[52] and optimized by DFT calculations. The energies of the most stable configurations for each concentration are plotted in **Figure 8a**. All of the intermediate configurations have negative binding energies, which reveal that no clustering occurs during adsorption process. Then the most stable configurations are used to calculate voltage. As we see from **Figure 8b**, the voltage profile can be divided into two regions, where the voltage drops rapidly from 1.05 to 0.55 V ($0 < x < 0.333$), then decreases slowly from 0.55 to 0.46 V ($0.333 < x < 1$). The positive average voltage in each stage demonstrates the stable adsorption of Na during the charge/discharge process. Furthermore, the no-negative voltage profile also indicates that the half-cell reaction can take place spontaneously,

Table 2. Comparison of penta-h22 with previous studied anode materials for SIBs.

Materials	Specific capacity [mAh g ⁻¹]	Diffusion barrier [eV]	OCV [V]	Volume change [%]	Electronic property
Penta-h22 (this work)	609	0.20	0.63	1.75	Metal
hC28 ^[2,23]	717	0.08	0.36	2.30	Metal
ISN ^[51]	159.5	0.01	1.35	2.80	Semimetal
T-C ₂₄ ^[50]	232.65	0.05	0.54	0.94	Semimetal
1T-MoS ₂ ^[53]	86	0.28	1.25	27.5	Metal
2H-MoS ₂ ^[53]	146	0.68	0.75	27.1	Semiconductor
HZGM-42 ^[24,26]	318.5	0.08	0.43	1.85	Semimetal
YS ₂ ^[55]	350	0.24	1.44	–	Metal
Bco-C24 ^[56]	743.8	0.08	0.06	2.27	Semimetal

and the fully Na-intercalation configuration (Na_xC_{3.67}) can be achieved. Therefore, the average voltage of penta-h22 is 0.63 V, which is lower than ISN (1.35 V)^[51] and 2H-MoS₂ (0.75 V).^[53]

To evaluate the cycling stability, we calculate the volume change during the charge/discharge process defined as $\Delta V = [(V_{\text{Na}} - V_0)/V_0] \times 100\%$, where V_{Na} and V_0 are the volume of fully/no Na-intercalated penta-h22 configurations, respectively. The volume change of penta-h22 is found to be 1.75%, which is smaller than hC28 (2.30%),^[2] HZGM-42 (1.85%),^[26] and C-honeycomb (within 15%).^[54] The reason of the low volume change should be correlated to the high Young's modulus of penta-h22 in *c* direction and the large pore with a diameter of 12.02 Å, which is larger than C-honeycomb (10.39 Å)^[54] and hC28 (11.83 Å).^[2]

For clarity, comparisons are made for measuring the anode performance for SIB between penta-h22 and other previously reported systems as listed in Table 2. One can see that for capacity, energy barrier, voltage, and volume change, penta-h22 shows well-balanced performance.

4. Conclusions

In summary, we propose a new stable 3D porous metallic carbon structure composed of interlocking pentagons containing sp²- and sp³-hybridized carbon atoms, penta-h22, and its metallicity is found to come from the delocalized electrons of sp² carbon as confirmed by DOS as well as ELF. Equally important, different from the previously reported T6-carbon with interlocking hexagons, the 3D pentagon-interlocking porous carbon exhibits excellent performance for SIB anode with the following important results: 1) High specific capacity of 609 mAh g⁻¹ without clustering. 2) Low energy barrier of 0.17–0.20 eV because of the unique configuration of penta-h22. The low diffusion barrier together with the intrinsically high electronic conductivity can enhance the rate capability of penta-h22. 3) The average open-circuit voltage is 0.63 V, which is comparable with many anode materials.^[51,53] 4) The volume change is considerably small, suggesting that penta-h22 has a good cycling stability during charging and discharging. This work clearly shows that pentagon-based materials are promising for battery applications.

Acknowledgements

This work was partially supported by grants from the National Natural Science Foundation of China (Grant Nos. NSFC-11974028 and NSFC-21773004), the National Key Research and Development Program of the Ministry of Science and Technology of China (2017YFA0205003), and was supported by the High Performance Computing Platform of Peking University, China.

Conflict of Interest

The authors declare no conflict of interest.

Data Availability Statement

The data that support the findings of this study are available from the corresponding author upon reasonable request.

Keywords

carbon anodes, DFT, interlocking carbon pentagons, sodium-ion batteries

Received: January 25, 2021

Revised: April 1, 2021

Published online:

- [1] R. Hoffmann, A. A. Kabanov, A. A. Golov, D. M. Proserpio, *Angew. Chem., Int. Ed.* **2016**, *55*, 10962.
- [2] W. Zhou, H. Xie, S. Wang, Q. Wang, P. Jena, *Carbon* **2020**, *168*, 163.
- [3] A. H. Castro Neto, F. Guinea, N. M. R. Peres, K. S. Novoselov, A. K. Geim, *Rev. Mod. Phys.* **2009**, *81*, 109.
- [4] S. Iijima, *Nature* **1991**, *354*, 56.
- [5] H. W. Kroto, J. R. Heath, S. C. O'Brien, R. F. Curl, R. E. Smalley, *Nature* **1985**, *318*, 162.
- [6] H. Terrones, M. Terrones, E. Hernández, N. Grobert, J. C. Charlier, P. M. Ajayan, *Phys. Rev. Lett.* **2000**, *84*, 1716.
- [7] Y. Huang, M. Okada, K. Tanaka, T. Yamabe, *Phys. Rev. B* **1996**, *53*, 5129.
- [8] Y. Wu, J. Maultzsch, E. Knoesel, B. Chandra, M. Huang, M. Y. Sfeir, L. E. Brus, J. Hone, T. F. Heinz, *Phys. Rev. Lett.* **2007**, *99*, 027402.
- [9] T. Hertel, G. Moos, *Phys. Rev. Lett.* **2000**, *84*, 5002.
- [10] S. Piscanec, M. Lazzeri, J. Robertson, A. C. Ferrari, F. Mauri, *Phys. Rev. B* **2007**, *75*, 035427.

- [11] C. Bergeret, J. Cousseau, V. Fernandez, J.-Y. Mevellec, S. Lefrant, *J. Phys. Chem. C* **2008**, *112*, 16411.
- [12] C. G. Rocha, A. Latgé, L. Chico, *Phys. Rev. B: Condens. Matter Mater. Phys.* **2005**, *72*, 085419.
- [13] S. Zhang, Q. Wang, X. Chen, P. Jena, *Proc. Natl. Acad. Sci. USA* **2013**, *110*, 18809.
- [14] H. Prinzbach, A. Weiler, P. Landenberger, F. Wahl, J. Wörth, L. T. Scott, M. Belmont, D. Olevano, B. V. Issendorff, *Nature* **2000**, *407*, 60.
- [15] M. Saito, Y. Miyamoto, *Phys. Rev. Lett.* **2001**, *87*, 035503.
- [16] S. Zhang, J. Zhou, Q. Wang, X. Chen, Y. Kawazoe, P. Jena, *Proc. Natl. Acad. Sci. USA* **2015**, *112*, 2372.
- [17] X. Zhu, H. Su, *J. Phys. Chem. C* **2017**, *121*, 13810.
- [18] X. Li, J. Liu, F. Q. Wang, Q. Wang, P. Jena, *J. Phys. Chem. Lett.* **2019**, *10*, 6360.
- [19] J. Liu, S. Wang, Q. Sun, *Proc. Natl. Acad. Sci. USA* **2017**, *114*, 651.
- [20] J. Liu, S. Wang, Y. Qie, C. Zhang, Q. Sun, *Phys. Rev. Mater.* **2018**, *2*, 025403.
- [21] X. Wang, Z. Feng, J. Rong, Y. Zhang, Y. Zhong, J. Feng, X. Yu, Z. Zhan, *Carbon* **2019**, *142*, 438.
- [22] Z. Pang, X. Gu, Y. Wei, R. Yang, M. S. Dresselhaus, *Nano Lett.* **2017**, *17*, 179.
- [23] J. Hu, W. Wu, C. Zhong, N. Liu, C. Ouyang, H. Y. Yang, S. A. Yang, *Carbon* **2019**, *141*, 417.
- [24] J. Liu, X. Li, Q. Wang, Y. Kawazoe, P. Jena, *J. Mater. Chem. A* **2018**, *6*, 13816.
- [25] N. V. Krainyukova, E. N. Zubarev, *Phys. Rev. Lett.* **2016**, *116*, 055501.
- [26] Y. Shen, Q. Wang, Y. Kawazoe, P. Jena, *J. Power Sources* **2020**, *478*, 228746.
- [27] G. Kresse, J. Furthmüller, *Phys. Rev. B* **1996**, *54*, 11169.
- [28] J. P. Perdew, K. Burke, M. Ernzerhof, *Phys. Rev. Lett.* **1996**, *77*, 3865.
- [29] J. Heyd, G. E. Scuseria, M. Ernzerhof, *J. Chem. Phys.* **2003**, *118*, 8207.
- [30] H. J. Monkhorst, J. D. Pack, *Phys. Rev. B* **1976**, *13*, 5188.
- [31] S. Curtarolo, W. Setyawan, G. L. W. Hart, M. Jahnatek, R. V. Chepulskii, R. H. Taylor, S. Wang, J. Xue, K. Yang, O. Levy, M. J. Mehl, H. T. Stokes, D. O. Demchenko, D. Morgan, *Comput. Mater. Sci.* **2012**, *58*, 218.
- [32] A. Togo, F. Oba, I. Tanaka, *Phys. Rev. B* **2008**, *78*, 134106.
- [33] K. Parlinski, Z. Q. Li, Y. Kawazoe, *Phys. Rev. Lett.* **1997**, *78*, 4063.
- [34] S. Nosé, *J. Chem. Phys.* **1984**, *81*, 511.
- [35] G. Mills, H. Jónsson, *Phys. Rev. Lett.* **1994**, *72*, 1124.
- [36] S. Grimme, *J. Comput. Chem.* **2006**, *27*, 1787.
- [37] M. J. Bucknum, R. Hoffmann, *J. Am. Chem. Soc.* **1994**, *116*, 11456.
- [38] K. M. Merz, R. Hoffmann, A. T. Balaban, *J. Am. Chem. Soc.* **1987**, *109*, 6742.
- [39] C.-X. Zhao, C.-Y. Niu, Z.-J. Qin, X. Y. Ren, J.-T. Wang, J.-H. Cho, Y. Jia, *Sci. Rep.* **2016**, *6*, 21879.
- [40] Y. Cheng, R. Melnik, Y. Kawazoe, B. Wen, *Cryst. Growth Des.* **2016**, *16*, 1360.
- [41] C.-Y. Niu, X.-Q. Wang, J.-T. Wang, *J. Chem. Phys.* **2014**, *140*, 054514.
- [42] S. H. Zhang, R. F. Zhang, *Comput. Phys. Commun.* **2017**, *220*, 403.
- [43] M. E. Kilic, K.-R. Lee, *Carbon* **2021**, *174*, 368.
- [44] M. Born, K. Huang, *Dynamical Theory of Crystal Lattices*, Clarendon Press, Oxford **1954**.
- [45] V. A. Gorodtsov, D. S. Lisovenko, *Mech. Mater.* **2019**, *134*, 1.
- [46] Y. Zhang, H. Sun, C. Chen, *Phys. Rev. Lett.* **2004**, *93*, 195504.
- [47] A. D. Becke, K. E. Edgecombe, *J. Chem. Phys.* **1990**, *92*, 5397.
- [48] W. Tang, E. Sanville, G. Henkelman, *J. Phys.: Condens. Matter* **2009**, *21*, 084204.
- [49] C. Uthaisar, V. Barone, *Nano Lett.* **2010**, *10*, 2838.
- [50] Y. Qie, J. Liu, S. Wang, Q. Sun, P. Jena, *J. Mater. Chem. A* **2019**, *7*, 5733.
- [51] Y. Qie, J. Liu, X. Li, S. Wang, Q. Sun, P. Jena, *Phys. Rev. Mater.* **2018**, *2*, 084201.
- [52] S. P. Ong, W. D. Richards, A. Jain, G. Hautier, M. Kocher, S. Cholia, D. Gunter, V. L. Chevrier, K. A. Persson, G. Ceder, *Comput. Mater. Sci.* **2013**, *68*, 314.
- [53] M. Mortazavi, C. Wang, J. Deng, V. B. Shenoy, N. V. Medhekar, *J. Power Sources* **2014**, *268*, 279.
- [54] L. Shi, A. Xu, T. Zhao, *J. Phys. Chem. C* **2018**, *122*, 21262.
- [55] Y. Guo, T. Bo, Y. Wu, J. Zhang, Z. Lu, W. Li, X. Li, P. Zhang, B. Wang, *Solid State Ionics* **2020**, *345*, 115187.
- [56] S. Wang, B. Yang, E. Ruckenstein, H. Chen, *Carbon* **2020**, *159*, 542.